

***BeppoSAX* Observations of the Power and Energy Spectral Evolution in *the* Black Hole Candidate XTE J1650-500**

Enrico Montanari¹, Lev Titarchuk^{1,2} and Filippo Frontera³

ABSTRACT

We study the time variability and spectral evolution of the Black Hole Candidate source XTE J1650-500 using the *BeppoSAX* wide energy range (0.12-200 keV) observations performed during the 2001 X-ray outburst. The source evolves from a low/hard state (LHS) toward a high/soft state (HSS). In all states the emergent photon spectrum is described by the sum of Comptonization and soft (disk) blackbody components. In the LHS, the Comptonization component dominates in the resulting spectrum. On the other hand, during the HSS observed by *BeppoSAX* the soft (disk) component is already dominant. In this state the Comptonization part of the spectrum is much softer than that in the LHS (photon index Γ is ~ 2.4 in the HSS vs. $\Gamma \sim 1.7$ in the LHS). In the *BeppoSAX* data we find a strong signature of the index saturation with the mass accretion rate which can be considered as an observational evidence of the converging flow (black hole) in XTE J1650-500. We derive power spectra (PS) of the source time variability in different spectral states as a function of energy band. When the source undergoes a transition to softer states, the PS as a whole is shifted to higher frequencies which can be interpreted as a contraction of the Compton cloud during hard-soft spectral evolution. It is worthwhile to emphasize a detection of a strong low-frequency red noise component in the HSS PS which can be considered a signature of the presence of the strong extended disk in the

¹Dipartimento di Fisica, Università di Ferrara, Via Saragat 1, I-44100 Ferrara and IIS Calvi, Finale Emilia (MO), Italy; montana@fe.infn.it

²George Mason University/Center for Earth Observing and Space Research, Fairfax, VA 22030; US Naval Research Laboratory, Code 7655, Washington, DC 20375-5352; Goddard Space Flight Center, NASA, code 663, Greenbelt MD 20771 USA; Dipartimento di Fisica, Università di Ferrara, Via Saragat 1, I-44100 Ferrara, Italy; lev.titarchuk@nrl.navy.mil

³Dipartimento di Fisica, Università di Ferrara, Via Saragat 1, I-44100 Ferrara, Italy and INAF/IASF, Bologna, Via Gobetti 101, I-40129, Bologna, Italy; frontera@fe.infn.it;

HSS. Also as a result of our data analysis, we find a very weak sign of K_α line appearance in this *BeppoSAX* data set. This finding does not confirm previous claims by Miniutti et al. on the presence of a broad and strongly relativistic iron emission line in this particular set of *BeppoSAX* data.

Subject headings: accretion, accretion disks—black hole physics—stars: individual (XTE J1650-500): radiation mechanisms: nonthermal—physical data and processes

1. Introduction

XTE J1650-500 was discovered by the Rossi X-Ray Timing Explorer (*RXTE*) on 2001 September 5 (Remillard et al. 2001) and subsequently reached a peak X-ray intensity of 0.5 crab. Subsequent observations established that XTE J1650-500 is a strong black hole candidate based on its X-ray spectrum and variability in the X-ray light curve (Markwardt et al. 2001; Revnivtsev & Sunyaev 2001; Wijnands et al. 2001; Homan et al. 2003; Kalemci et al. 2003; Rossi et al. 2004). The radio counterpart was discovered with the Australia Telescope Compact Array (ATCA) by Groot et al. (2001). Further radio observations sampled the behavior of XTE J1650-500 along all its X-ray states (Corbel et al. 2004). Orosz et al. (2004) found the period of the binary system to be 7.63 ± 0.02 h, and the mass function [low limit of black hole (BH) mass] to be $2.7 \pm 0.6 M_\odot$.

We define the spectral state hardness according to the peak position in the $EF(E)$ -diagram related to X-ray spectrum $F(E)$ (in units of $\text{erg keV}^{-1}\text{s}^{-1}$) where E is the photon energy [see e.g. Figure 3 in Grove et al. (1998)]. Following this definition, we call a low/hard state (LHS) the spectral state in which the maximum of the $EF(E)$ -diagram is located at tens of keV, while we call a high/soft state (HSS) the state where the $EF(E)$ -maximum is located at a few keV. Moreover, we call an intermediate state (IS) the state in which the source undergoes a spectral transition between the low/hard and high/soft states. We observed XTE J1650-500 three times with *BeppoSAX* during the 2001 outburst (September 11–12, 21–23, October 3–4, see Table 1), during which the source evolves from the LHS toward the HSS. The observed outburst is a perfect case to study a source transition from the LHS to the HSS.

The long-term monitoring of Cyg X-1 has revealed not only two distinct energy spectra and transitions between them but it has also established that the corresponding time variability power spectra (PS) evolve along with the photon spectra [see Shaposhnikov & Titarchuk (2006), hereafter ST06, and Shaposhnikov & Titarchuk (2007), hereafter ST07]. Recently

the evolution of the power density spectra throughout the different X-ray states of BH X-ray binaries has been also extensively studied in many BHs by Klein-Wolt & van der Klis (2008), hereafter KVK08.

The persistence of the simultaneous PS and X-ray energy spectrum evolution suggests that the underlying physical process and conditions which give rise to the PS are tied to the corona; and, furthermore, that this process varies in a well defined manner as the source progresses from one spectral state to another.

Moreover the same evolutions are seen in so many galactic X-ray binary BH sources (see, for example, detailed discussion of these evolutions in Cyg X-1, GRO 1655-40 and GRS 1915+ 105 in ST07) which vary widely in both luminosity (presumably with mass accretion rate) and state. This fact suggests that the physical conditions controlling the photon spectral and the PS evolutions are similar. In particular, quasiperiodic oscillation (QPO) frequencies are characteristics of the power spectra for these sources. Given that correlations between low and high frequency QPOs and between low frequency QPOs and break frequencies in their PS have been found for a number of them (see Psaltis et al. 1999; Belloni et al. 2002), one can suggest that QPO phenomenon can be an universal property of all accreting compact systems.

In particular, the PS of black hole binaries in hard states is dominated by a component, which has a specific shape roughly described by a broken power-law (BKNPL). The low-frequency part of the BKNPL is mostly flat, while the higher frequency part above the “break” frequency ν_{br} is a power law $\nu^{-\alpha}$ which index α varies between 1 and 2. In fact, the PS of BHs are more complicated than just a broken power law [see Titarchuk et al. (2007), Titarchuk & Shaposhnikov (2008), hereafter TSA07, TS08 respectively, and KVK08 for comprehensive study of the BH power density spectra in different X-ray spectral states].

It is also well established that the fractional root-mean-square (rms) variability in a source light curve decreases while QPO low-frequency (and ν_{br}) increases as the source evolves from the LH state to the HS state [see e.g. TS08, KVK08].

Lyubarskii (1997) was the first to suggest a model for this time variability production in the accretion powered X-ray sources. He considered small amplitude local fluctuations in the accretion rate at each radius, caused by small amplitude variations in the viscosity, and then studied the effect of these fluctuations on the accretion rate at the inner disc edge. His linear calculations show that if the characteristic time-scale of the viscosity variations is everywhere comparable to the viscous (inflow) time-scale, and if the amplitude of the variations is independent of radius, then the power spectrum of luminosity fluctuations is a power-law of index $\alpha = 1$, namely $\propto \nu^{-1}$. If the amplitude of the variations increases

with radius, the slope of the power spectrum of the luminosity variations α is steeper than 1. Lyubarskii pointed out that he had no physical model for the cause of such fluctuations. Uttley, McHardy & Vaughan (2005) pointed out that rms-flux relation is naturally explained in the framework developed by Lyubarskii.

TSA07 formulated and solved the problem of local driving perturbation diffusion in a “disk-like” configuration (which can be either a geometric thin Keplerian accretion disk or a Compton cloud). The problem of the diffusive propagation of the spatially distributed high-frequency perturbations is formulated as a problem in terms of the diffusion equation for the surface density perturbations. This equation is combined with the appropriate boundary conditions. The formulation of this problem and its solution are general and classical. The emergent power spectrum as a result of the perturbation diffusion in a given bounded configuration (either Compton cloud or Keplerian disk) has a white-red noise (WRN) shape which can be approximated by a broken power-law (BKNPL) with two indices 0 and $\alpha \gtrsim 1$ respectively. The parameters of the WRN PS are a timescale of the diffusion propagation of the local perturbations t_0 and the power-law index of the viscosity distribution over radius.

Note that the shapes of X-ray photon spectra of black hole (BH) and neutron star (NS) are generic: they consist of Comptonized blackbody-like (BB) components. These Comptonization components are seen as a power-law (PL) at energies higher than the BB characteristic energies. Sometimes one needs an exponential rollover in order to terminate the PL component at high energies. The main difference is that NS spectra are usually softer for the same state. Another difference in these spectra is that in the NS case there are two Comptonized BB components (not one as in BHC spectra) which can be related to the emission from the disk (BB color temperature about 1 keV) and NS surface (BB color temperature about 2.5 keV [see Titarchuk, & Shaposhnikov (2005)]).

Titarchuk et al. (1997), hereafter TMK97, introduced the Generic Comptonization model (BMC model in XSPEC) that takes into account the dynamical Comptonization (converging inflow, expected in the vicinity of the central object) along with the thermal Comptonization. Note that this model can be applied to fit the observed spectra of NS and BHC sources.

In this Paper we present the results of our evolution study of the energy and power spectra in XTE J1650-500 using the *BeppoSAX* observations and using the aforementioned theoretical considerations of photon and power spectral formations. *We find that this evolution is similar to that observed from Cyg X-1* (see e.g. ST06 and TSA07).

Miniutti et al. (2004), hereafter M04, reported spectral results from three *BeppoSAX* observations of XTE J1650-500 during its 2001/2002 outburst. By performing the analysis

in the energy range from 1.5 to 60 keV for the TOO-1 spectrum and in the range from 1.5 to 200 keV for the other two spectra, they reported the presence of a broad and strongly relativistic Fe K_α line with an EW of about 200 eV, depending on TOO. We reanalyze the same *BeppoSAX* data set adopting the entire BeppoSAX energy range (0.12–200 keV) in order to check the presence of a strong K_α line in the data. We find a very weak sign of K_α line appearance.

Results of our detailed spectral analysis are the subject of our next paper (Montanari et al. 2008 in preparation). Here we present results on the simultaneous evolution of the spectral and temporal properties and compare them with that in other black hole (BH) sources (see ST06 and ST07).

Our approach is two-fold: On one side we tried to fit all photon and power spectra with the same generic simple model, in order to compare them directly. On the other hand, we study the source in the framework of a physical model in the attempt to find a self-consistent scenario that can help us to understand the Physics of the spectral and timing evolution that we observe.

In §2 we briefly describe the *BeppoSAX* data from XTE J1650-500. Details of our spectral fitting are presented in §3. We discuss an observational evidence of a converging flow in §3.1. We present the results of our analysis of K_α appearance in the data in §3.2. Description of XTE J1650-500 power spectra and QPO identification are presented in §4 where we also discuss a correlation of PS vs spectral state (photon index) revealed in XTE J1650-500. Discussion and conclusions follow in §5.

2. Observations and data reduction

XTE J1650-500 was observed on September 11–12, 21–23 and October 3–4 2001 during three Target of Opportunity Observations (TOOs) by the Narrow Field Instruments (NFIs) on board *BeppoSAX* (Boella et al. 1997a). Table 1 reports the observation log along with the on–source exposure times. The NFIs include a Low–Energy Concentrator Spectrometer (LECS, 0.1–10 keV; Parmar et al. 1997), three Medium–Energy Concentrator Spectrometer (MECS, 1.5–10 keV; Boella et al. 1997b), a High–Pressure Gas Scintillation Proportional Counter (HPGSPC, 4–120 keV; Manzo et al. 1997), and a Phoswich Detection System (PDS, 15–200 keV; Frontera et al. 1997). The SAXDAS data analysis package is used for processing data.

For each instrument we perform the spectral and temporal analysis in the energy range in which the response function is well determined; given the high statistics of the source the

energy range is 0.12–4.0 keV for the LECS, 2.5–10 keV for the MECS, 8–30 keV for the HPGSPC, and 15–200 keV for PDS. Note that, at the given high count rate, the available LECS response function is not reliable, therefore the SAX/LECS Matrix Generation Program “lemat” is used to obtain the appropriate response function of the instrument. MECS unit 1 was not operative. Spectra from MECS unit 2 and 3 are merged. The spectra so obtained are rebinned taking into account the energy resolution of the instruments in order to get independent data points.

Previously M04 analyzed the same set of *BeppoSAX* data integrating the source spectra over the entire duration of each of the three observations. However, this integration time could provide distorted spectra, given that the source shows a significant spectral variability with time on shorter time scales. This effect was first revealed studying the time variability of three different hardness ratios $R[(4 - 10)\text{keV}/(2 - 10)\text{keV}]$, $R[(10 - 30)\text{keV}/(2 - 10)\text{keV}]$, $R[(20 - 60)\text{keV}/(2 - 10)\text{keV}]$ with bins of 200 s integration time. The results, that will be reported in detail elsewhere (Montanari et al. 2008, in preparation), show that, depending on the epoch, significant (up to 30%) spectral variability is present in time intervals ranging from 1 to 10 ks. Therefore, unlike M04, we integrated the spectra over the longest time intervals compatible with a negligible (less than 5%) source spectral variability.

Namely, in the TOO-1 the spectra were divided in 12 time intervals and numerated from I101 to I112, in the TOO-2 they were divided in 19 intervals (from I201 to I219), while in the TOO-3 they were divided in 8 intervals (from I301 to I308). Note that LECS data are not available for five intervals of TOO-2.

In Figure 1 we display the source light curve related to the period from September 11 to October 4, 2001 for the 2–3 keV and 20–60 keV energy bands. The integration time of each bin is that of the IDs intervals used for spectral analysis. In Figure 1 one can clearly see an overall anti-correlation between the two light curves related to these two energy bands during TOO1 and TOO-2. Note that the transition to a softer spectrum becomes prominent in TOO-2 and continues during TOO-3 observations. For TOO-2 (see Fig. 1), a variable rate is evident at low energies, unlike an almost stable count rate at high energies. This different time behaviour at different energies can be also seen from Fig. 2 where we compare the energy behavior of MECS mean count rates in the time intervals I202 and I207.

We model the energy spectra using XSPEC 11.2.0 software package (Arnaud 1996). A systematic error of 1% is added in order to take into account unavoidable uncertainties in the response functions. In the multi-instrument fits we leave free to vary the relative normalization of LECS, HPGSPC and PDS with respect to MECS and the derived unfolded spectra are renormalized to the MECS level for a clarity of display.

For the temporal analysis we use standard fast Fourier techniques. Source PSs are normalized to rms units using subtraction of the Poissonian noise level. Dead time corrections have been taken into account according to van der Klis (1989). The binning time for the analysis is a few ms. PSs are calculated using data stretches of ~ 100 s and then averaged. In this way we obtain the reliable PSs in a frequency range from 0.01 to 100 Hz. Unfortunately we cannot provide much longer time stretches to extend the frequency pass band to lower values due to frequent interruptions in the data rate. We present only data points which are statistically significant (see more details in §4).

The uncertainties of the model parameters are given at 90% confidence level, while those shown in all figures are 1σ errors.

3. X-ray energy continuum spectra

In our analysis, all derived spectra (39) cover the 0.12–200 keV energy band, except 5 intervals in which the LECS data are not available. In this case the energy band was from 2.5 to 200 keV.

To describe the continuum spectrum we use the Bulk Motion Comptonization model (BMC in XSPEC) (Titarchuk et al. 1997) which is a *generic Comptonization model*. This model can be used if the photon energy is less than the mean electron energy of the Compton cloud E_{av} . The choice of this particular theoretical model is provided by the robust nature of the BMC model for different spectral states and independence of the specific type of Comptonization scenario involved. The BMC model spectrum is the sum of a blackbody (BB) component (which is the disk radiation directly seen by the observer) and the fraction of a BB component Comptonized in the corona.

The model has four parameters: the color temperature kT_{bb} of a thermal photon spectrum (blackbody, BB), the energy spectral index $\alpha = \Gamma - 1$, where Γ is the PL photon index, the parameter A , which is related to the weight $[A/(1 + A)]$ of the Comptonization component, and the normalization of the BB component C_N . The BMC model is valid for the general case of Comptonization when both bulk and thermal motion are included.

For the thermal Comptonization, E_{av} is related to electron temperature $E_{av} \sim 2kT_e$. When the bulk motion Comptonization is dominant, E_{av} is related to the bulk kinetic energy of the electrons $E_{av} \lesssim m_e c^2$. In the thermal Comptonization case, for energies less than E_{av} , COMPTT¹ and BMC models are very similar. The thermal Comptonization and the

¹COMPTT model was introduced by Titarchuk (1994), Titarchuk & Lyubarskij (1995) and

dynamical (bulk motion) Comptonization are presumably responsible for the spectral formation in the hard state and the soft state, respectively. Therefore, one needs a general model such as the BMC that describes the spectral shape regardless of the specific type of Comptonization. Although the thermal Comptonization model can properly fit the spectral shape of the observed spectra for all spectral states, it would give physically unreasonable values of the best-fit parameters for the soft state spectra. Notably, Wilms et al. (2006) found optical depth τ of the Compton Cloud inferred from the COMPTT model that significantly decreases towards the HSS. It is very difficult (in the framework of any reasonable physical model) to justify this tendency of τ to decrease when the mass accretion rate increases during the hard-to-soft state transition (see e.g. ST06). However the spectral index α inferred using the best-fit COMPTT parameters τ and kT_e is a physical characteristic of the Comptonization process. In fact, the spectral index α is the reciprocal of the Comptonization parameter Y [see e.g. Bradshaw et al. (2007)] and it is independent of any type and model of Comptonization (thermal or bulk).

It is important to emphasize the principal difference and similarity in using blackbody-like spectra (BBODY in XSPEC) and multicolor disk spectra (DISKBB IN XSPEC) as soft photon spectra. In fact, Borozdin et al. (1999), hereafter BRT99, demonstrated that in a limited energy range (for example *RXTE*/PCA) the DISKBB is fit by a BB spectrum. The color BB temperature is the best-fit parameter which is related to the effective radius of the emission area of the disk. It is evident that the best-fit values of the color temperature and effective radius depend on the energy range of the instrument (see BRT99). Any disk model requires the integral of the local spectra over radius. These local emergent spectra are not necessarily blackbody-like spectra and they are indeed formed as a result of the radiative transfer effects which depend on the assumption of the local density and temperature structure. Moreover the specific diskBB model assumes a temperature distribution with the disk radius that is likely not the real distribution. Thus, taking all that into account, we have preferred to describe the thermal (BB-like) component of the source spectrum by adding another BB to that *already* included in the BMC model.

Following XSPEC notation, the model used to describe our spectra is given by $F(E) = WABS \times (BBODY + BMC) \times SMEDGE \times HIGHECUT$. Here WABS is the XSPEC photoelectric absorption model which takes into account a possible intrinsic photoelectric absorption in the source and/or external absorption of X-ray source emission in the way towards the Earth. The *BMC* Comptonization model describes both direct (from an innermost part of the disk) and Comptonized photons (from the corona), the added BBODY component

Hua & Titarchuk (1995) to describe the spectrum of thermal Comptonization in the whole energy range.

describes the direct soft photons belonging to the disk part at a greater distance from the central object which spectrum can be only slightly affected by upscattering in the corona. The SMEDGE (smeared K-edge) model represents a possible interaction of the photons originated in the inner part of the X-ray source with a wind (see Laurent & Titarchuk 2007). The HIGHECUT (high-energy cutoff) model enables to take into account the curvature effect of the Comptonized photon spectrum at high energies (that is above 100 keV in the LHS spectra) due to the recoil effect which is neglected by BMC. HIGHECUT is found to be needed to describe the LHS energy spectrum, while, for the HSS, no high energy cutoff is needed.

Most of the 39 spectra are found to be very well fit by the assumed input model. Only for 9 spectra the model has a null hypothesis probability less than 0.05, with 3 of them with null hypothesis probability less than 0.01, the smallest value being 3.7×10^{-3} .

The best-fit parameters of 6 typical spectra extracted from the entire set are shown in Table 2. As can be seen, the temperature kT_{sbb} of the soft blackbody varies from 0.18 to 0.36 keV, while that of the BMC, kT_{bb} , varies in the range from 0.39 to 0.56 keV, depending on the spectral state. For the same time intervals of Table 2, we show in Fig. 3 the best fit $EF(E)$ spectra in $\text{keV cm}^{-2} \text{ s}^{-1}$ units. In the LHS spectra I105 and I111 the relevant Comptonization contribution is related to the thermal Comptonization of soft (disk) photons off hot electrons of Compton cloud (corona). Instead, in the HSS spectra (see spectra I215, I216, I303, and I306 in Fig. 3), the blackbody emission (both BBs), presumably related to the intrinsic disk spectrum, is dominant in the resulting spectrum, while the hard (steep PL) photons, probably formed in the relatively cold (a few keV temperature) compact region, are only a small fraction of the total flux.

As we noted above, the use of the thermal Comptonization model (COMPTT) is physically justified for the fitting of the LHS spectra only. For comparison with the results reported in Table 2, for time intervals I105 and I111 we implemented a fit using a model $WABS \times (BB + COMPTT) \times SMEDGE$ (see Table 3). In fact, the fit quality obtained using the COMPTT model are not so good as that in the case of BMC [compare the $\chi^2/(\text{dof})$ values in Table 2 and 3] presumably because a modest converging flow contribution to the overall Compton upscattering is already present in TOO1. In general, the worse quality fits introduce additional systematic errors in the best-fit model parameters. In particular, the photon index, obtained using COMPTT best-fit optical depth τ and electron temperature kT_e and using the formula for the index related to τ and kT_e [see Titarchuk & Lyubarskij (1995)], is 0.4 higher than that inferred using BMC.

In the sections 4–5 we present the arguments for the compactness of the steep PL emission region which is presumably *a converging flow* streaming towards the *innermost part of the BH*.

3.1. Observational evidence of the converging flow (black hole) in XTE J1650-500

It is important to emphasize once again (see above) that the spectral index α ($=\Gamma - 1$) is the reciprocal of the Comptonization parameter Y [see e.g. Bradshaw et al. (2007)] and it is independent of the Comptonization model (thermal or bulk). The parameter $Y = N_{sc}\eta$ is the mean number of scatterings N_{sc} times the average fractional energy change per scattering η . The number of scatterings of Comptonized (upscattered) photons in the converging flow (CF) N_{sc} is proportional to the optical depth τ , given that in the converging flow the photons can be only effectively upscattered in the direction of the bulk motion, and thus $N_{sc} \propto R/l = \tau$, where R is the CF characteristic radius and l is the photon free path. It is also worth noting that, in the converging flow, τ is also equal to the dimensionless mass accretion rate $\dot{m} = \dot{M}/\dot{M}_{\text{Ed}}$ where \dot{M}_{Ed} is defined as $\dot{M}_{\text{Ed}} = L_{\text{Ed}}/c^2$ [see Titarchuk et al. (1997) for more details]. On the other hand, the change of the CF fractional energy per scattering η is inversely proportional τ ($\eta \propto 1/\tau$) when $\tau \gg 1$ [see for more details in Laurent & Titarchuk (2007)].

Consequently $Y = N_{sc}\eta$ and thus $\Gamma = 1/Y + 1$ saturate to a constant value when τ (or \dot{m}) increases. Observationally this index saturation can be revealed if one can find a correlation between Γ and BMC normalization $C_N = L_{39}/d_{10}^2$ where $L_{39} = L_d/(10^{39} \text{ erg s}^{-1})$ is the luminosity of the seed photon source (disk) in units of $10^{39} \text{ erg s}^{-1}$ and d_{10} is the distance to source in units of 10 kpc. This correlation of the index Γ with $C_N = L_{39}/d_{10}^2$ implies the correlation of Γ vs \dot{m} given that L_d as a disk luminosity is proportional to \dot{m} , namely $L_d \propto \varepsilon_{eff} m \dot{m}$, where $m = M/M_\odot$ is the black hole mass in units of solar mass and ε_{eff} is the efficiency of the gravitational energy release in the accretion disk [see e.g. Shakura & Sunyaev (1973)]. In principle, the efficiency ε_{eff} can depend on the inner radius of the disk $R_{in,d}$, i.e. indirectly depends on \dot{m} . However, in HSS, $R_{in,d}$ presumably reaches its lowest limit of about $3R_S$ [see e.g. Shrader & Titarchuk (1999)] and thus, in HSS, the index vs. C_N correlation is equivalent to the correlation between index and \dot{m} . This implies that in HSS the index saturation with C_N is equivalent to the index saturation with \dot{m} .

In Figure 4 we present an observational evidence of the index saturation with L_{39}/d_{10}^2 , and thus with \dot{m} , which can be considered as *an observational signature of a converging flow (black hole) in XTE J1650-500*.

3.2. On iron fluorescence line determination

Limiting our considerations to the *BeppoSAX* TOOs we confirm the broad excess at ~ 6.4 keV found by M04 in all of the three observations if we adopt, as M04 did, the XSPEC reflection model PEXRIV. However, the excess is present only in the first TOO if we use a two-phase accretion disk corona model which also includes the reflection effect (XSPEC COMPSS Model) (Montanari et al. 2008, in preparation). It is worth noting that when we use COMPSS model we find a strange effect (unexpected in the scenario described by this model) that the iron line (thought to be due to reflection from the disk) is present when the reflection parameter is low (in TOO1) and it is completely absent when the reflection parameter becomes larger (in TOO2 and TOO3) (see Montanari et al. 2004). Also as we have already mentioned above, in the framework of the COMPSS model there is a puzzling effect of significant decrease of the optical depth of the Compton cloud when the source evolves to the HSS (Montanari et al. 2004).

On the other hand, using the input continuum model described in Section 3 and the entire *BeppoSAX* spectral energy range we find a very marginal evidence for the presence of the Fe fluorescence line in the data. We illustrate our findings in Figure 5.

Adopting the 0.12–200 keV energy range, the fit of the continuum model $WABS \times (BB + BMC) \times SMEDGE \times HIGHENCUT$ to the spectrum I108, used as an example, is shown in the panel 2 (starting from the top). As can be seen, the above continuum model gives a very satisfactory description of the data ($\chi^2/\text{dof} = 150/164$), with no need of adding a Fe K_α line model. Instead the *SMEDGE* model appears crucial for a good fit. The fit of the above continuum model with no *SMEDGE* to the same spectrum (see top panel) is highly unacceptable ($\chi^2/\text{dof} = 430/165$). The apparent sinusoidal pattern of the residuals to the model is a clear sign of the bad fit quality.

Note the addition of a K_α line (LAOR model) to the continuum model with no *SMEDGE* gives an unacceptable fit ($\chi^2/\text{dof} = 300/163$) (see panel 3), but it becomes acceptable ($\chi^2/\text{dof} = 136/109$, see panel 5), if we limit the spectrum energy bandwidth to 1.5–60 keV (the band used by M04)². However the model which is valid in 1.5–60 keV, is not valid in the entire *BeppoSAX* energy band. Namely the model $WABS \times (BB + BMC + LAOR) \times HIGHENCUT$, with the best-fit parameter values found for the 1.5–60 keV energy band, does not fit the data related to the entire *BeppoSAX* energy range from 0.12 to 200 keV ($\chi^2/\text{dof} = 1315/164$, see panel 6).

²Note that a fit of the model $WABS \times (BB + BMC) \times HIGHENCUT$ with no Laor component does not fit the data in this limited energy band (see panel 4).

We have also attempted to understand why M04, using the *SMEDGE* model as we do, obtained different results. Limiting the analysis to the spectrum I108, assumed as an example, we actually find that, freezing the energy of the Edge to the best-fit value reported by M04 [$E_{edge} = 8.3$ keV being consistent with a very high ionization state of iron (*ion XXII*), see Kallman et al. (2004)] gives the presence of a significant emission line. The line disappears when E_{edge} is left free to vary, finding, as a best-fit value, 7.2 keV.

To conclude, iron K_α line appearance strongly depends on the energy band used to describe the continuum emission. With our best-fit continuum model, that gives the best description of the source spectrum in the entire 0.1–200 keV *BeppoSAX* energy band, *the line is not required*.

Although no significant emission line is evident in the data, adding the XSPEC LAOR model to our best-fit model (see Section 3) slightly improves the fits ($\Delta\chi < 10$ with a decrease of 4 dof for about 160 initial dof) for some observation intervals belonging to TOO1 (LHS). The resulting line, of equivalent width ranging from few tens eV to about 100 eV, *is almost symmetric* with its center being situated in the energy range between 5 and 5.5 keV. For all of other intervals the normalization of the line goes to zero.

Concerning the *SMEDGE* model used in the best fit description of our spectra, it is worth noting there is a relation between Thompson optical depth τ_T of the iron emission area and the *SMEDGE* maximum absorption optical depth τ_{max} at threshold [see Basko (1978) and ST06]:

$$\tau_{max} = (Y + Y_0) \tau_T \left(\frac{7.8 \text{ keV}}{E_{th}} \right)^3 \quad (1)$$

where Y and Y_0 (in units of the cosmic values) are the abundances of the elements with a charge $Z < 26$ and the iron abundance respectively, while E_{th} is the K-shell ionization threshold energy. In our case $Y \simeq 1$, $Y_0 \simeq 1$, $E_{th} = 7.1$ keV, so

$$\tau_{max} \simeq 2.65\tau_T$$

For instance, $\tau_{max} = 2, 3, 4, 5$ correspond to $\tau_T = 0.75, 1.1, 1.5, 1.9$ respectively.

We find that, in the LHS, the Thomson optical depth τ_T is relatively low, i.e. about 0.7 whereas, in the HSS, τ_T is about 2 (see Table 2 for the values of τ_{max} and Eq. 1 for the $\tau_{max} - \tau_T$ relation). Thus, while in the LHS the possible detection of the line is consistent with the value of the Thompson optical depth $\tau_T \sim 0.7$ (see Table 2), in the HSS, its non detection is consistent with the smearing due to a significant Thompson optical depth τ_T in the range between ~ 1.3 and ~ 2 (see above).

One can ask a fair question on the relation between the K-edge and K_α appearances in the data. In many models K_α -line formation is indeed strongly related to edge formation

[see e.g. Basko et al. (1974), Basko (1978), Kallman et al. (2004), Laming & Titarchuk (2004), Laurent & Titarchuk (2007)]. However it is not always true that the detection of the K-edge in the data implies the K_α –line detection. The physics of the K-edge and K_α formation is the following: photons of energies higher than 7.1 keV ionize the iron K-shell and this ionization effect leads to emission of K_α –photon (iron K_α –fluorescence) with a probability of $\omega_K \lesssim 0.3$ (where ω_K is K-yield), whereas with probability $(1 - \omega_K)$ the K_α energy goes to an ionized electron. So the edge can be always there but the K_α –photon is emitted with a probability less than 0.3 and in addition this probability is affected by the electron density of the surrounding medium (see more details in the aforementioned references on this subject). Even if the K_α –photon is emitted it does not mean that this photon can be detected and seen by the Earth observer. These photons can be absorbed when they propagate through the medium (for example in the wind) and they can be also scattered off electrons and significantly change their energy, i.e. washed out from the resulting spectrum. All these effects of line appearance and disappearance have been reproduced in simulations by Laming & Titarchuk (2004) and Laurent & Titarchuk (2007).

4. Power spectrum and timing-spectral correlation

We succeeded to derive accurate power spectra (PS) of the source time variability thanks to the high source brightness during outburst. In particular, during TOO-1, when the source was mainly in the LHS, it was possible to obtain the PS in several energy intervals within the broad 0.1–200 keV *BeppoSAX* operational band.

4.1. Phenomenological (Lorentzian) Model

First we made the analysis of the power spectra using, as an input model, the superposition of Lorentzian functions (Lorentzian model). We compared their characteristics with those identified by KVK08 for a number of BHs. A Lorentzian function is given by

$$L(\nu) = K \frac{\hat{\Gamma}/2\pi}{(\nu - \nu_0)^2 + (\hat{\Gamma}/2)^2} \quad (2)$$

where ν_0 is the centroid frequency and $\hat{\Gamma}$ is the full width at half maximum of the function (FWHM).

We used broad Lorentzians to fit the continuum spectrum and narrow Lorentzians to fit QPO features. In Figure 6 (*bottom panel*) we illustrated the fitting results and the

characteristics of the PS components in terms of frequency×power diagram. Note the power spectrum unit is $(rms/mean)^2/Hz$ and thus the frequency ×power unit is $(rms/mean)^2$. Below we presented a comparison of these characteristics with those found by KVK08.

The continuum of all derived LHS PSs is found to be well described by the sum of two broad Lorentzians L_1 and L_2 . Following the KVK08 notation, we formally call them L_b and L_h , respectively. We report the best fit characteristic frequency of these broad Lorentzians in Table 4. This frequency corresponds to the maximum of the $\nu L(\nu)$ diagram $\nu_{max} = [\nu_0^2 + (\hat{\Gamma}/2)^2]^{0.5}$. The presented PSs are results of integration over the entire duration of each TOO.

Using Fig. 6 and Table 4 one can see that, in addition to the two broad Lorentzians L_b and L_h , the 2-10 keV power-frequency diagram of the LHS (TOO1) requires two narrow Lorentzians: a low frequency (LF) QPO and a higher frequency QPO at $\nu_{QPO1} \sim 1.5$ Hz and $\nu_{QPO2} \sim 3$ Hz, respectively. These two QPOs were introduced by KVK08 as LF and LF⁺, respectively. Note that $\nu_{QPO2} \sim 3$ Hz (or LF⁺) was found to be consistent with the second harmonics of ν_{QPO1} (or LF).

However, in the 0.1–2 keV energy channel, no evidence of ν_{QPO2} is found and the characteristic frequency of the broad Lorentzian L_h , that describes the hump to the right of the QPO frequency (see blue line in the right bottom panel of Fig. 6), is at 23 Hz. Note the L_h –hump is located at ~ 2 Hz in the 2–10 keV power-frequency diagram.

In Table 5 we show the energy dependence of the LHS PS components in the broad energy bands from 0.1-2 keV to 15–200 keV. The characteristic frequencies of L_b are consistent with each other up to 15 keV and the L_h characteristic frequencies are consistent with each other in the 2–4, 4–10 and 8–15 keV energy intervals. Using the $L_b - L_h$ relation found (for the energy band 2-25 keV) by Wijnands and van der Klis [Wijnands & van der Klis (1999)], updated in KVK08, we find that our medium energy data points are consistent with that relation. Also the PS narrow components L_{QPO1} and L_{QPO2} clearly detected in the 4-10 keV and 8-15 keV bands satisfy the Wijnands and van der Klis $L_{LF} - L_b$ relation (see Fig. 10 in KVK08).

It is worth noting that, in the 0.1–2 keV and 15-200 keV energy intervals, the L_h frequencies are an order of magnitude higher than those at medium energies. In fact, it is the first time that the high values of ν_{max} (~ 23 Hz, > 50 Hz in the 0.1–2.0 keV and 15–200 keV energy bands respectively), are discovered from this source. Their identification with the L_h introduced by, e.g., by KVK08, is not obvious. Unfortunately, there are no data in the literature to statistically study a possible correlation between L_b and L_h at these energies, unlike what can be done at medium energies with RXTE data (see, e.g., KVK08). The L_h

components in the 0.1–2 keV and 15–200 keV energy bands can be related to PS physical components which are different from that in the medium energy bands (see details of the physical interpretation in section 4.2).

In the HSS, the PS continuum is still found to be well described by the sum of two broad Lorentzians, but in this case (see Table 4 and Fig. 6), L_h is no more visible, while a very low frequency noise (VLFN) emerges. It is important to emphasize that the characteristic frequency of L_b increases from the LHS to the HSS. Our finding is in agreement with the fact that the L_b characteristic frequency is shifted to higher values during the source evolution from the LHS to the HSS [see also Fig. 4 in KVK08]. We also confirm the KVK08 result that LFN component occurs in the HSS, but is absent in LHS [compare our Fig. 6 (*bottom panels*) with panels *a* and *e* in Fig. 4 of KVK08].

Furthermore we find that the Q-value, defined as $Q = \nu_0/\hat{\Gamma}$, is in the range of 0–0.5 for L_b , L_h components and that is in the range of 4–6 for PS narrow components L_{QPO} . As one can see from Fig. 6 that *rms*/mean values are 10% and 30% for L_b and L_h of the LHS power spectra components respectively in 0.1-2 keV. The corresponding *rms*/mean values for the LHS L_b and L_h in 2-10 keV band are about 10% (see left bottom panel of Fig. 6). However the variability power of the PS components drastically decreases in the HSS, and their rms-values are less than 1%. It is worth noting that these ranges of Q and rms values are consistent with that found by KVK08 (see Table 1 there).

4.2. Physical (diffusion) model

The analysis of the PSs was performed using a simplified version of the diffusion model (see TSA07 and TS08) in which the PS continuum shape at frequencies below the driving frequency can be approximated by a broken power-law (BKNPL). The results of the model fitting to the data are shown in Tables 6-8. We also present the model fitting results in Figs. 6-7.

In particular, in Fig. 7 and Table 6 we show the energy dependence of the LHS PSs and the variability power, that decreases with energy (mainly above 10 keV), while it preserves the self-similar shape for energies higher than 2 keV. These results obtained for the LHS have relevant implications. The self-similar shape of the > 2 keV spectra implies that photons of these energies are produced (upscattered) in the same geometrical configuration. Following TSA07, the break frequency found in the LHS PSs is related to a diffusion time of perturbation propagation while the QPO low frequency is an eigenfrequency of the volume (magnetoacoustic) oscillation of the medium (in our case it is a Compton cloud). Our results

show that the values of these PS characteristics are similar in all PSs for photon energies higher than 2 keV.

As we have already demonstrated in Section 3, the energy spectral behaviour (Fig. 3), even within TOO-1, shows a slight softening from the time interval I105 to I111. In order to see the effect of this softening in the PS, we have compared the 4–10 keV PS derived in the time interval from I101 to I107 with that related to the time interval from I109 to I112 in the 4–10 keV energy band. Note that the 4–10 keV band was chosen because we find the best signal to noise ratio *in this interval*.

The result is presented in Table 7 and in Fig. 8. The main effect shown in Fig. 8 is the shift to higher frequencies of the PS which correlates with the photon spectral softening (see Fig. 3). Independently of the continuum adopted model the LF QPO centroid frequency increases while the continuum noise remains stable in its shape. For the diffusion model continuum, as can be seen from Table 7, the LF QPO frequency increases from 1.47 ± 0.03 Hz to 1.66 ± 0.08 Hz (uncertainties at 90% confidence level).

In order to illustrate the evolution of the power spectra from TOO-1 to TOO-2, when the energy spectra undergo their transition from the LHS to the HSS (see I215 and I216 spectra in Fig. 3), we compared the LHS PS with the HSS PS in two energy bands where the signal is highest: 2-10 keV and 0.1-2 keV (see top left and top right panels of Fig. 6, respectively). As can be seen from this Figure, the relative power of the HSS PS (with respect to the LHS PS) and its shape strongly depend on the energy band.

We find (see Table 8) that the 0.1–2 keV HSS PS is well described by the sum of a PL plus a BKNPL, with no evidence of QPOs in contrast to the 0.1–2 keV LHS PS which is described (see Table 6) by a BKNPL plus a high ($\nu_0 \sim 14$ Hz) frequency broad Lorentzian (FWHM ~ 40 Hz). On the other hand the 2–10 keV HSS PS (see Table 8 and Fig. 6) can be fit with a PL with plus a constant, while the 2–10 keV LHS PS is fit with a BKNPL plus two narrow Lorentzians, one of which is consistent to be the second harmonics of the other at $\nu_0 \sim 1.5$ Hz.

These results confirm what was previously found by Homan et al. (2003) using *RXTE* data, that there are prominent QPO features in XTE J1650-500 PSs [see also Revnivtsev & Sunyaev (2001) and Wijnands et al. (2001)].

In the LHS, the Comptonization component is dominant and thus we should detect the X-ray emission along with its variability related to the Comptonizing region (Compton cloud) only. Indeed in all of the LHS PSs shown in Fig. 6, the VLFN component is not seen. *Its absence is in agreement with the low intensity level of the direct disk blackbody component in the LHS energy spectra* (see I105 and I111 spectra in Fig. 3). It is important to emphasize

that, in the LHS, the typical values of the characteristic frequencies of the VLFN and BKNPL components are of the order of $10^{-7} - 10^{-6}$ Hz and $0.1 - 1$ Hz, respectively (see TSA07 for Cyg X-1 case and KVK08). Thus, in this spectral state, the disk variability can be clearly detected only if frequencies lower than 10^{-3} Hz corresponding to photon energies less than ~ 0.1 keV (see TSA07). However this is not the case for *BeppoSAX*.

On the other hand in the HSS PSs the VLFN component appears (with the power depending on the energy range) along with the BKNPL component. Note that this latter component is barely visible in the 2–10 keV PS (see Fig. 6). This result is in agreement with a low contribution of the high energy tail in the HSS energy spectra (see Fig. 3). Following TSA07, we can interpret the VLFN component observed in the HSS as related to the timing response of the extended disk, while BKNPL or L_b (in terms of Lorentzian model) is associated with mass accretion rate perturbations in the Compton cloud (see the HSS PS in the right panels of Fig. 6).

We find that in the 0.1–2 keV band not only $\nu_{b,max}$ (using the Lorentzian model) but also ν_{br} (using the diffusion model) increase from TOO–1 (LHS) to TOO–2 (HSS) by a factor 60 ($\nu_{b,max}$ increases from $0.59_{-0.13}^{+0.06}$ Hz to 36 ± 3 Hz, while ν_{br} increases from 0.28 ± 0.03 Hz to $\sim 17_{-2}^{+7}$ Hz). This high shift of the related frequencies is in agreement with the corona (Compton cloud) contraction during the LHS-HSS transition (see TSA07). Searching in the literature, we found that in Cyg X-1 PSs the break frequency changes from ~ 0.03 Hz to ~ 18 Hz value when photon index varies from 1.5 to 2.1 (see Fig. 8 in ST06). Also we should point out that Wijnands & van der Klis (1999) (see Fig. 2) reported the range for the break frequency in BHs is $0.03 - 30$ Hz.

The ~ 14 Hz hump clearly seen in the 0.1-2 keV LHS PS (see Fig. 6 and Tables 4, 6) disappears at higher energies presumably because of the lack of statistics (compare with Fig. 7). TSA07 and TS08 give an explanation of this hump in the high frequency tail of the power spectrum of Cygnus X–1, in terms of driving frequency of the perturbation oscillations of the Compton cloud.

5. Discussion and Conclusions

In this Paper we present the results of simultaneous spectral and timing analysis of the BHC XTE J1650-500 observed by *BeppoSAX*.

The energy spectra are well described by the sum of a Comptonization and soft blackbody components along with a smeared edge. In particular, we argue that the iron line appearance strongly depends on the energy band used to describe the continuum emission.

Using both the high energy (>20 keV) and the low energy (<1.5 keV) bands, which are both crucial to describe the real continuum level, the presence of the iron line feature is not mandatorily required. Thus we conclude that the line feature is not so prominent in *BeppoSAX* data as initially reported by M04. One may also attribute the difference of our conclusion regarding the presence of the K_α –iron line in the *BeppoSAX* data and that by M04 to a different treatment of systematic errors and different procedure of data integration over time.

We find the clear evidence of an evolution of the spectra from the LHS to the HSS (see Fig. 3). In the LHS the Comptonization component dominates, in contrast to the HSS when the blackbody component dominates the emergent spectrum. Moreover in the *BeppoSAX* data (see Fig. 4) we find a strong signature of the index saturation with BMC normalization L_{39}/d_{10}^2 , which is, in fact, proportional to the disk mass accretion rate. *This index saturation vs. mass accretion rate can be considered as an observational evidence of the converging flow (black hole) in XTE J1650-500 [Titarchuk & Zannias (1998) and Titarchuk, & Fiorito (2004) hereafter TF04].*

The relative contribution of the Comptonization component (in the resulting spectrum) decreases when the source undergoes the hard-to-soft spectral transition (see Fig. 3). We interpret this as a result of contraction of the Comptonization region (Compton cloud) during this spectral evolution [see Titarchuk et al. (1998), hereafter TLM98, and TF04].

We can infer this contraction effect using our best-fit model parameters. One of the parameters of the BMC model is the normalization of the blackbody (BB) component C_N which is directly related to the effective area A_{bb}^{eff} of the BB emission [$A_{bb}^{eff} \propto C_N/(T_{bb}^4(1+A))$]. If we multiply this effective area with the fraction of Comptonized component $f = A/(1+A)$, we obtain the effective area of the high energy X–ray emission region (the Compton cloud). Using the best-fit values for the LHS and HSS spectra we find that the area of the Compton cloud decreases by a factor five during the transition from the LHS to the HSS (see Fig. 9).

Furthermore in Fig. 10 we demonstrate how the Comptonization fraction f decreases when the photon index increases. This correlation presents one more argument for a Compton cloud contraction during LHS-HSS evolution. While in §4 we argued this contraction effect using the power spectrum analysis only, here we find more arguments for this contraction using the energy spectrum analysis.

Actually the power spectra follow the energy spectral evolution. The PSs related to the softer energy spectra are weaker and shifted to higher frequencies with respect to those related to the harder spectra. It leads us to the conclusion that the emission area (CC) does

contract when the source undergoes the hard-to-soft state transition.

Furthermore TLM98 argued that the size of CC strongly depends on the Reynolds (Re) number of the accretion flow, and not on just the mass accretion rate. In other words, the LHS-HSS transition should be dictated by Re-number values, which is low in the LHS and high in the HSS, and the CC size decreases when Re-number increases. TS08 check this TLM98 prediction using Cyg X-1 observations by *RXTE*. First, they find a method to infer the Re-number of the accretion flow using the observations. Then they demonstrate that when Re-number increases all characteristic frequencies of the power spectrum are indeed shifted to higher values as a result of Compton cloud contraction during the LHS-HSS transition.

It is well known from the observations of X-ray BH binaries [see e.g. Wijnands & van der Klis (1999), ST06, ST07 and KVK08] that the power spectra evolve along with the photon spectra. Here we find that our results for XTE J1650-500 are related to the findings by ST06 for Cyg X-1, where the authors, analyzing ~ 10 years of observational data from *RXTE* archive, found strongly correlated characteristics of power spectra and photon spectra (photon index). We have to admit that our claims of temporal and spectral correlation in XTE J1650-500 are based on only the limited set of the *BeppoSAX* data, while the results of the extensive *RXTE* data set for XTE J1650-500 by Shaposhnikov & Titarchuk (2008), hereafter ST08, do indicate a strongly correlated temporal and spectral evolution in this source.

This suggests that the underlying physics of the radiative and oscillatory processes is common in X-ray BH binaries. The consistency of the Comptonization model also suggests that their spectra emerge from similar Compton cloud geometric configurations whose sizes shrink during the state transition. The disk becomes more powerful at softer states and the cooling of Compton cloud is mostly dictated by the strong soft disk emission. The photon field and surrounding plasma are almost in equilibrium: the plasma temperature is the same order of the photon blackbody color temperature (of a few keV). The converging flow located in the innermost part of compact cloud is the only place where photons can be upscattered to energies of order of $m_e c^2$ and higher due to the dynamical Comptonization.

In the HSS PSs we see the presence of two noise components: VLNF and BKNPL (or L_{VLNF} and L_b in terms of Lorentzian model). We suggest that the VLNF component is associated with the extended disk and BKNPL is presumably formed as a result of the diffusive propagation of the mass accretion rate perturbation in the compact Compton cloud. In the LHS PSs only BKNPL is observed, while the VLNF related to the disk component, presumably very weak and at very low frequencies, cannot be observed in the *BeppoSAX* data.

We also show that in XTE 1650-500 the power of X-ray variability drastically decreases

towards the HSS. Note this effect have been known for a number of BHs (see KVK08 and TS08 for details of the observations and explanation of this effect, respectively). The relative power of the HSS PS with respect of that in the LHS clearly depends on the energy bands. We present (for the first time in the literature) energy-dependent PSs of X-ray emission using *BeppoSAX* data. While we find a noticeable dependence of the PS strength on energy, the PS shape is found to be almost self-similar in different energy bands (at least for the LHS PSs).

Moreover, we show that the break and QPO low frequencies of the XTE J1650-500 PSs which we derived, correlate with the spectral state, in particular with the PL photon index of the energy spectrum. We succeed to determine the LF QPO corresponding to two different LHS spectra (indices): $\nu_{QPO} = 1.47 \pm 0.05$ Hz, 1.66 ± 0.08 Hz related to $\Gamma = 1.74 \pm 0.01$ and 1.79 ± 0.06 respectively. Thus our data points based on *BeppoSAX* data for XTE J1650-500 are consistent with the index-QPO correlation found by ST08, based on the *RXTE* data for XTE J1650-500.

We would like to thank anonymous referees for constructive suggestions to significantly improve the paper presentation.

REFERENCES

- Arnaud, K. A. 1996, ASP Conf. Series, 101, 17
- Basko, M. M., Sunyaev, R.A. & Titarchuk, L.G. 1974, A&A, 31, 249
- Basko, M. M. 1978, ApJ, 223, 268
- Belloni, T., Psaltis, D., & van der Klis, M 2002, ApJ, 572, 392
- Boella, G., Butler, R. C., Perola, G. C., Piro, L., Scarsi, L., Bleeker, J. A. M., 1997a, A&AS, 122, 299
- Boella, G., Chiappetti, L., Conti, G., Cusumano, G., del Sordo, S., La Rosa, G., Maccarone, M. C., Mineo, T., Molendi, S., Re, S., Sacco, B., Tripiciano, M., 1997b, A&AS, 122, 327
- Borozdin, K., Revnivtsev, M., Trudolyubov, S., Shrader, C. & Titarchuk, L. 1999, ApJ, 517, 367
- Bradshaw, C. F., Titarchuk, L., & Kuznetsov, S. 2007, ApJ, 663, 1225

- Corbel, S., Fender, R. P., Tomsick, J. A., Tzioumis, A. K., & Tingay, S. 2004, *ApJ*, 617, 1272
- Frontera, F., Costa, E., dal Fiume, D., Feroci, M., Nicastro, L., Orlandini, M., Palazzi, E., Zavattini, G., 1997, *A&AS*, 122, 357
- Gies, D. R., & Bolton, C. T. 1982, *ApJ*, 260, 240
- Groot, P., Tingay, S., Udalski, A., & Miller, J. 2001, *IAU Circ.*, 7708, 4
- Grove, J. E., Johnson, W.N., Kroeger, R. A., McNaron-Brown, K. & Skibo, J.G. 1998, *ApJ*, 500, 899
- Homan, J. et al. 2003, *ApJ*, 586, 1262
- Hua, X-M., & Titarchuk, L. 1995, *ApJ*, 449, 188
- Kalemci, M. et al. 2003, *ApJ*, 586, 419
- Kallman, T.R., Palmeri, P., Bautista, M.A., Mendoza, C. & Krolik, J.H. 2004, *ApJS*, 155, 675
- Klein-Wolt, M. & van der Klis, M. 2008, *ApJ*, 675, 1407 (KVK08)
- Laming, J.M. & Titarchuk, L. 2004, *ApJ*, 615, 121
- Laurent, P. & Titarchuk, L. 2007, *ApJ*, 656, 1056
- Leahy, D. A., Darbro, W., Elsner, R. F. et al. , 1983, *ApJ*, 266, 160
- Lyubarskii, Yu., E. 1997, *MNRAS*, 292, 679
- Manzo, G., Giarrusso, S., Santangelo, A., Ciralli, F., Fazio, G., Piraino, S., & Segreto, A. 1997, *A&AS*, 122, 341
- Markwardt, C., Swank, J., & Smith, E. 2001, *IAU Circ.*, 7707, 2
- Miller, J. M., Fabian, A. C., Wijnands, R., Reynolds, C. S., Ehle, M., Freyberg, M. J., van der Klis, M., Lewin, W., H., G., Sanchez–Fernandez, C., & Castro–Tirado, A. J. 2002, *ApJ*, 570, L69
- Miller, J. M. et al. 2004, *ApJ*, 606, L131
- Miniutti, G., Fabian, A. C., & Miller, J. M. 2004, *MNRAS*, 351, 466 (M04)

- Montanari, E., Frontera, F., & Amati, L. 2004, *Nucl. Phys. B Proc. Suppl.*, 132, 412
- Orosz, J. A., McClintock, J. E., Remillard, R. A., & Corbel, S., 2004, *ApJ*, 616, 376
- Parmar, A. N., Martin, D. D. E., Bavdaz, M., Favata, F., Kuulkers, E., Vacanti, G., Lam-
mers, U., Peacock, A., & Taylor, B. G., 1997, *A&AS*, 122, 309
- Psaltis, D., Belloni, T., & van der Klis, M 1999, *ApJ*, 520, 262
- Remillard, R. A. 2001, *IAU Circ.*, 7707, 1
- Revnivtsev, M., & Sunyaev, R. 2001, *IAU Circ.*, 7715, 1
- Rossi, S., Homan, J., Miller, J. M., & Belloni, T. 2005, *MNRAS*, 360, 763
- Rossi, S., Homan, J., Miller, J. M., & Belloni, T. 2004, *NuPhS*, 132, 416
- Shakura, N.I., & Sunyaev, R.A. 1973, *A&A*, 24, 337
- Shaposhnikov, N., & Titarchuk, L. 2007, *ApJ*, 663, 445 (ST07)
- Shaposhnikov, N., & Titarchuk, L. 2006, *ApJ*, 643, 1098 (ST06)
- Shaposhnikov, N., & Titarchuk, L. 2008, submitted to *ApJ*.
- Shrader, C., & Titarchuk, L.G. 1999, *ApJ*, 521, L121
- Titarchuk, L. 1994, *ApJ*, 434, 272
- Titarchuk, L., Kuznetsov, S. & Shaposhnikov, N. 2007, *ApJ*, 667,
- Titarchuk, L.G. & Fiorito, R. 2004, *ApJ*, 612, 988 (TF04)
- Titarchuk, L., Lapidus, I.I., & Muslimov, A. 1998, *ApJ*, 499, 315 (TLM98)
- Titarchuk, L., & Lyubarskij, Yu. 1995, *ApJ*, 450, 876
- Titarchuk, L., Mastichiadis, A., & Kylafis, N. D., 1997, *ApJ*, 487, 834
- Titarchuk, L. G., Mastichiadis, A., & Kylafis, N. D. 1996, *A&A*, 120, 171 (TMK96)
- Titarchuk, L.G. & Zannias, T. 1998, 493, 863
- Titarchuk, L.G. & Shaposhnikov, N. 2008, *ApJ*, 678, 1230 (TS08)
- Titarchuk, L.G., Shaposhnikov, N. & Arefiev, V. 2007, *ApJ*, 660, 556 (TSA07)

- Titarchuk, L.G. & Shaposhnikov, N. 2005, ApJ, 626, 298 (TS05)
- Uttley, P., McHardy, I.M., & Vaughan, S. 2005, MNRAS, 359, 345
- van der Klis, M. 1989, Timing neutron stars, ed. H. Ögelman, & E.P.J. van der Heuvel (Dordrech:Kluwer), NATO ASI Ser. C, 262, 27
- van der Klis, M. 1995, in X-ray binaries, ed. W.H.G. Lewin, J., van Paradijs, & E.P.J. van der Heuvel (Cambridge Univ. Press, Cambridge), p. 252
- Vignarca, F., Migliari, S., Belloni, T., Psaltis, D., & van der Klis, M. 2003, A&A, 397, 729 (V03)
- Wijnands, R., Miller, J. M., & Lewin, W. H. G. 2001, IAU Circ., 7715, 2
- Wijnands, R., van der Klis, M. 1999, ApJ, 514, 939
- Wilms, J., Nowak, M. A., Pottschmidt, K., Pooley, G. G., & Fritz, S. 2006, A&A, 447, 245

Table 1: Log of the three observations of XTE J1650-500

Obs.	Start time (UT)	End time (UT)	LECS	MECS	HPGSPC	PDS
			ks	ks	ks	ks
1	2001 Sep. 11 10:57:04	2001 Sep. 12 18:43:06	20.3	47.4	47.0	22.2
2	2001 Sep. 21 18:15:39	2001 Sep. 23 14:03:40	15.9	63.9	73.3	30.3
3	2001 Oct. 03 16:36:53	2001 Oct. 04 10:15:56	7.2	27.8	33.0	12.8

Table 2. Parameters of the model: $WABS \times (BBODY + BMC) \times SMEDGE \times HIGHECUT$. $HIGHECUT$ was used only for the LHS. Parameters not listed in the table were held fixed. For $HIGHECUT$: $E_{cut} = 10$ keV; for $SMEDGE$: $E_{edge} = 7.1$ keV, index for photo-electric absorption = 2.67 (default value), smearing width = 10 keV. Errors are given at the 90% confidence level.

Model	Parameters	I105	I111	I215	I216	I303	I308
WABS	N_H (10^{22} cm $^{-2}$)	$0.62^{+0.04}_{-0.07}$	$0.62^{+0.08}_{-0.07}$	$0.48^{+0.01}_{-0.02}$	0.49 ± 0.02	0.50 ± 0.03	0.52 ± 0.02
BBODY	kT_{sbb} (keV)	$0.19^{+0.02}_{-0.01}$	0.19 ± 0.02	$0.36^{+0.03}_{-0.01}$	0.35 ± 0.02	0.34 ± 0.03	0.33 ± 0.02
BMC	Γ	$1.74^{+0.01}_{-0.02}$	1.81 ± 0.02	$2.50^{+0.02}_{-0.03}$	2.38 ± 0.03	2.32 ± 0.08	2.34 ± 0.04
	kT_{bb} (keV)	$0.40^{+0.02}_{-0.01}$	0.39 ± 0.02	$0.56^{+0.06}_{-0.02}$	$0.55^{+0.04}_{-0.03}$	$0.52^{+0.03}_{-0.02}$	0.54 ± 0.02
	$\log A$	$0.30^{+0.08}_{-0.04}$	$0.20^{+0.08}_{-0.07}$	$-0.31^{+0.12}_{-0.05}$	$-0.44^{+0.07}_{-0.06}$	$-1.06^{+0.09}_{-0.06}$	$-0.83^{+0.07}_{-0.05}$
	N_{sbb}/N_{bb}	0.8 ± 0.4	$0.9^{+0.9}_{-0.5}$	$1.4^{+0.9}_{-0.4}$	$1.3^{+0.5}_{-0.3}$	$1.1^{+0.8}_{-0.4}$	$1.3^{+0.4}_{-0.3}$
SMEDGE	τ_{max}	$2.04^{+0.10}_{-0.13}$	$1.96^{+0.17}_{-0.19}$	$3.5^{+0.2}_{-0.4}$	$3.6^{+0.3}_{-0.4}$	$5.3^{+0.9}_{-1.0}$	$4.5^{+0.6}_{-0.5}$
HIGHECUT	E_F (keV)	114^{+5}_{-6}	114^{+8}_{-9}	—	—	—	—
	χ^2/dof	179.0/164	167.7/163	177.6/151	194.9/153	164.6/131	190.7/148

Table 3: Parameters of the model: $WABS \times (BBODY + COMPTT) \times SMEDGE$. Errors are given at the 90% confidence level.

Interval	I105	I111
N_H (10^{22} cm $^{-2}$)	$0.38^{+0.02}_{-0.01}$	$0.39^{+0.03}_{-0.02}$
kT_{sbb} (keV)	0.30 ± 0.01	0.31 ± 0.01
$T0$ (keV)	0.45 ± 0.03	$0.46^{+0.05}_{-0.04}$
τ	$1.33^{+0.06}_{-0.08}$	$1.20^{+0.11}_{-0.16}$
kT_e (keV)	31^{+2}_{-1}	32^{+4}_{-2}
Γ	2.15 ± 0.03	2.12 ± 0.06
N_{sbb}/N_{comptt}	$0.52^{+0.02}_{-0.01}$	$0.68^{+0.02}_{-0.01}$
SMEDGE- τ_{\max}	$1.74^{+0.08}_{-0.12}$	1.7 ± 0.2
χ^2/dof	237.0/165	210.4/164

Table 4. Characteristics of BH XTE J1650-500 variability components of the power spectrum for Low Hard State (TOO-1) and High Soft state (TOO-2) [see Fig. 6 (bottom panel) for the related power spectra]. The model is a superposition of two broad Lorentzians (L_b , L_h) plus one or two narrow Lorentzians (L_{QPO1} , L_{QPO2}). Parameters in square parentheses are frozen in the fits. Errors are given at the 90% confidence level. See text about the identification of the L_h component.

Components	0.1–2 keV	2–10 keV
Hard State (TOO1)		
L_b , ν_b <i>max</i> (Hz)	$0.59^{+0.06}_{-0.13}$	$0.38^{+0.08}_{-0.04}$
L_h , ν_h <i>max</i> (Hz) ^a	23 ± 2	$2.4^{+3.1}_{-0.3}$
VLNF, ν_{VLNF} <i>max</i> (Hz)
L_{QPO1} , ν_{QPO} 0 (Hz)	1.55 ± 0.08	1.53 ± 0.04
L_{QPO2} , ν_{QPO} 0 (Hz)	...	3.08 ± 0.07
Soft State (TOO2)		
L_b , ν_b <i>max</i> (Hz)	36 ± 3	[35]
L_h , ν_h <i>max</i> (Hz)
VLNF, ν_{VLNF} <i>max</i> (Hz)	$(5^{+5}_{-3}) \times 10^{-2}$	$(4.6^{+1.1}_{-1.5}) \times 10^{-4}$

^aSee section 4.1, for details about the identification of the L_h component in the 0.1–2 and 2–10 keV energy intervals

Table 5. Energy dependence of PS component characteristics in Hard state (TOO-1) for the Lorentzian model. Parameters in square parentheses are frozen in the fits. Errors are given at the 90% confidence level.

Components	0.1–2 keV	2–4 keV	4–10 keV	8–15 keV	15–200 keV
$L_b, \nu_{b,max}$ (Hz)	$0.59^{+0.06}_{-0.13}$	0.38 ± 0.06	$0.36^{+0.08}_{-0.04}$	$0.38^{+0.08}_{-0.06}$	$3.3^{+1.0}_{-0.9}$
$L_h, \nu_{h,max}$ (Hz) ^a	23 ± 2	2.1 ± 0.2	$2.5^{+1.7}_{-0.5}$	$3.5^{+1.4}_{-0.8}$	> 50
L_{QPO1}, ν_0 (Hz)	$1.54^{+0.07}_{-0.06}$	[1.54]	...
L_{QPO2}, ν_0 (Hz)	$3.03^{+0.10}_{-0.09}$	[3.03]	...

^aSee section 4.1 for details about the identification of the L_h component in the 0.1–2, 2–4, 4–10, 8–15 and 15–200 keV intervals

Table 6. Best model fit parameters used to fit the power spectra of TOO-1 in different energy bands. The model: BKNPL + LORENTZIAN1 + LORENTZIAN2. Parameters in square parentheses are frozen in the fits. Errors are given at the 90% confidence level.

Parameter	0.1–2 keV	2–4 keV	4–10 keV	2–10 keV	8–15 keV	15–200 keV
α_1	[0.]	[0.]	[0.]	[0.]	[0.]	[0.]
α_2	0.7 ± 0.1	1.20 ± 0.02	1.05 ± 0.04	1.098 ± 0.013	0.96 ± 0.03	0.49 ± 0.10
ν_{br} (Hz)	0.28 ± 0.03	0.345 ± 0.016	0.36 ± 0.03	0.35 ± 0.01	0.37 ± 0.04	0.4 ± 0.4
$\nu_{L1\ 0}$ (Hz)	14_{+3}^{-7}	1.49 ± 0.09	1.52 ± 0.04	1.53 ± 0.03	1.54 ± 0.04	1.54 ± 0.15
FWHM_{L1} (Hz)	30_{+18}^{-14}	1.1 ± 0.3	0.8 ± 0.3	0.9 ± 0.2	0.46 ± 0.18	1.1 ± 1.4
$\nu_{L2\ 0}$ (Hz)	...	$[2\nu_{L1}]$	$[2\nu_{L1}]$	$[2\nu_{L1}]$	$[2\nu_{L1}]$	$[2\nu_{L1}]$
FWHM_{L2} (Hz)	...	1.6 ± 0.8	0.9 ± 0.3	0.95 ± 0.28	1.1 ± 0.5	1 ± 1
χ^2/dof	76.6/86	144.1/140	117.8/106	192.6/182	95.9/68	8.6/13

Table 7. Best fit parameters of the models used to fit the power spectra in two different time intervals (I101–I107, I109–I112) of TOO-1 in 4–10 keV . Model: BKNPL + LORENTZIAN1 + LORENTZIAN2. Parameters in square parentheses are frozen in the fits. Errors are given at the 90% confidence level.

Parameter	I101–I107	I109–I112
α_1	[0.]	[0.]
α_2	0.961 ± 0.025	1.23 ± 0.12
ν_{br} (Hz)	0.35 ± 0.03	0.37 ± 0.07
ν_{L1} (Hz)	1.47 ± 0.03	1.66 ± 0.08
FWHM_{L1} (Hz)	0.63 ± 0.25	1.2 ± 0.7
ν_{L2} (Hz)	[$2\nu_1$]	[$2\nu_1$]
FWHM_{L2} (Hz)	0.5 ± 0.2	0.9 ± 0.6
χ^2/dof	110.4/107	32.6/42

Table 8. Best fit parameters of the models used to describe the power spectra of TOO-2 (HSS). In 0.1-2 keV, two models: 1st model: PL + BKNPL; 2nd model: PL + constant. The first index of the BKNPL was fixed to 0. In 2–10 keV. Errors are given at the 90% confidence level.

Model	Parameter	0.1–2 keV	2–10 keV
PL+BKNPL			
	α	1.0 ± 0.3	...
	N_{PL}	$(4.0^{+6.0}_{-2.5}) \times 10^{-4}$...
	α_1	[0.]	...
	α_2	$1.0^{+0.1}_{-0.3}$...
	ν_{br} (Hz)	17^{+7}_{-2}	...
	N_{BKNPL}	$(2.0^{+0.1}_{-0.4}) \times 10^{-3}$...
PL+CONST			
	α	...	2 ± 1
	N_{PL}	...	$(3^{+100}_{-1}) \times 10^{-8}$
	$CONST$...	$(1.29 \pm 0.35) \times 10^{-5}$
	χ^2/dof	126/102	16.6/20

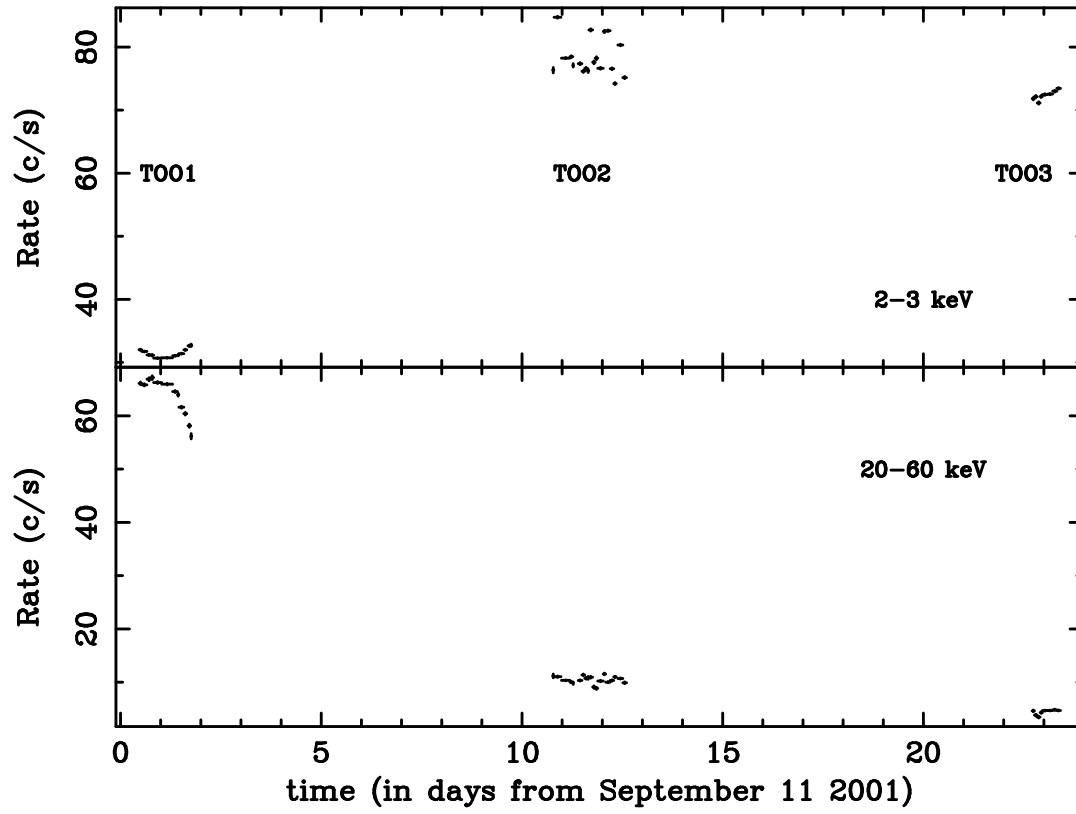


Fig. 1.— Light curves of XTE J1650-500 in two energy bands: 2-3 keV (*top*), 20-60 keV (*bottom*).

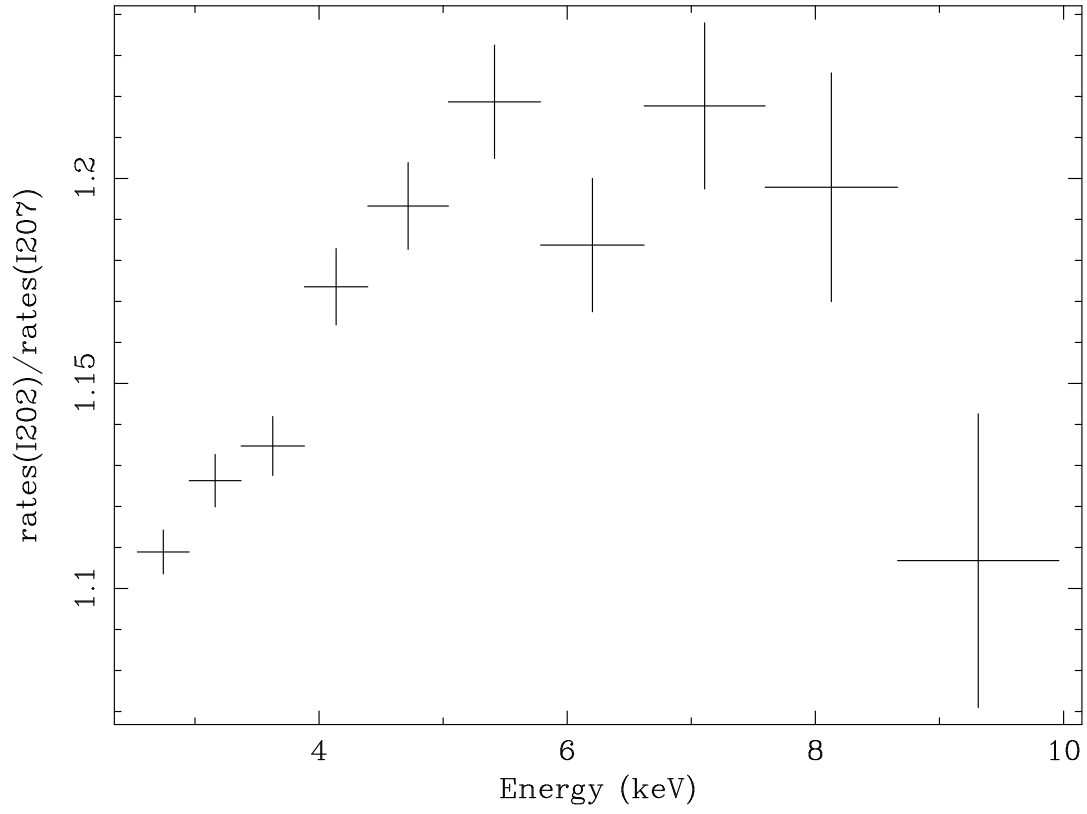


Fig. 2.— Ratio between MECS mean count rate in the time interval I202 (TOO-2) and that in interval I207 (TOO-2) as a function of energy.

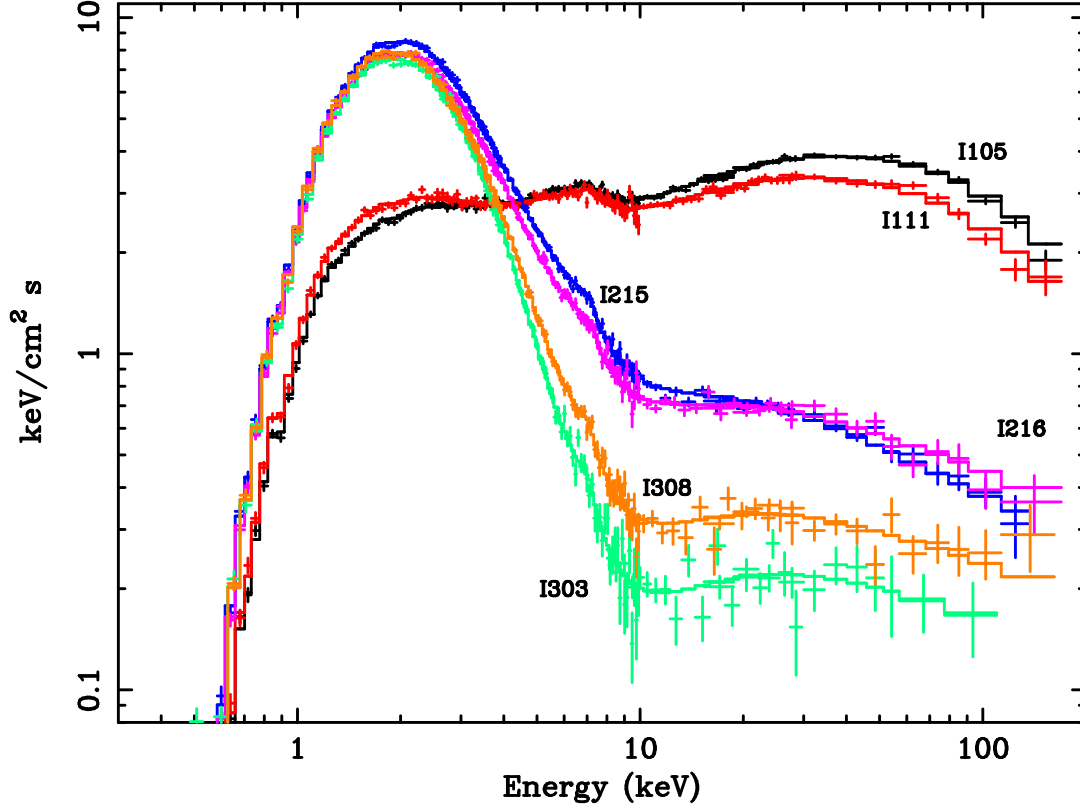
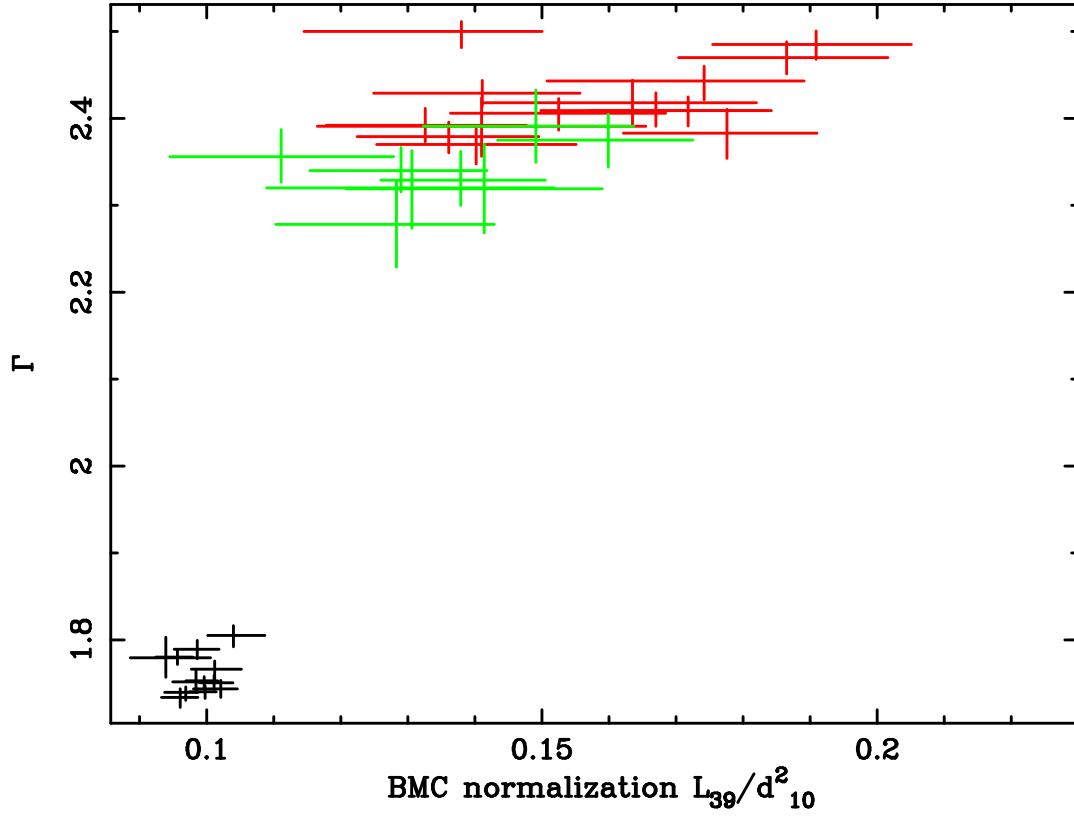


Fig. 3.— Evolution of the $EF(E)$ energy spectra with time. The LHS spectra (I105 and I111) show the key role of the thermal Comptonization of soft (disk) photons in the extended hot Compton cloud (corona), while the HSS spectra (I215–I216, I303, and I308) show that prominent contribution of the soft blackbody-like component due to the direct emission from the disk. In this case the hard X-ray component (i.e., the steep PL) is formed in the relatively cold (temperature of a few keV) compact region which is presumably a converging flow into the BH.



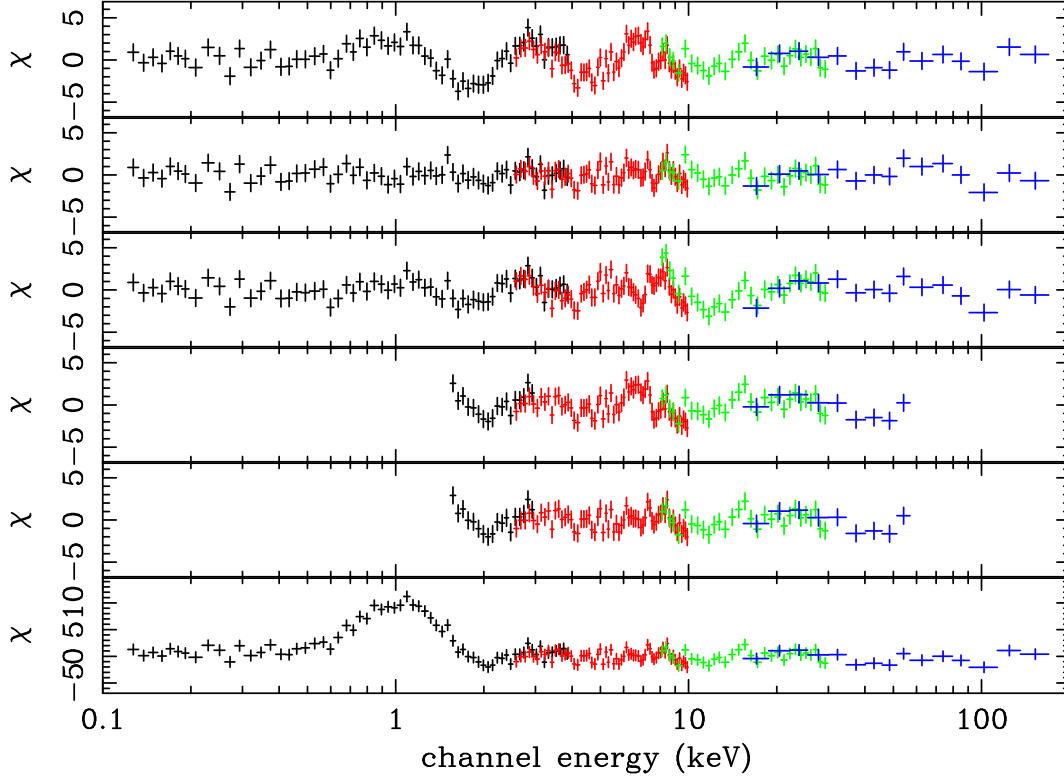


Fig. 5.— Residuals (in standard deviation units) of the source spectrum in the time interval I108 using different best-fit spectral models in different energy bands (see text). From top to bottom. *Panel 1*: XSPEC model $WABS \times (BB + BMC) \times HIGHENCUT$ fits to data in the 0.1-200 keV range, $\chi^2/(\text{dof})=430/165$. *Panel 2*: our best-fit model ($WABS \times (BB + BMC) \times SMEDGE \times HIGHENCUT$) fits to the same data, $\chi^2/(\text{dof})=150/164$. *Panel 3*: XSPEC model $WABS \times (BB + BMC + LAOR) \times HIGHENCUT$, $\chi^2/(\text{dof})=300/163$ fits to the data in the 0.1-200 keV. *Panel 4*: The same spectral model, adopted to fit the spectrum of panel 1, is used to fit the spectrum in the 1.5-60 keV, $\chi^2/(\text{dof})=200/111$. *Panel 5*: The same spectral model, adopted to fit the spectrum of panel 3, is used to fit the spectrum in the 1.5-60 keV energy range, $\chi^2/(\text{dof})=136/109$. *Panel 6*: The same model and parameters of panel 5, is used to fit the 0.1-200 keV energy range, $\chi^2/(\text{dof})=1315/164$.

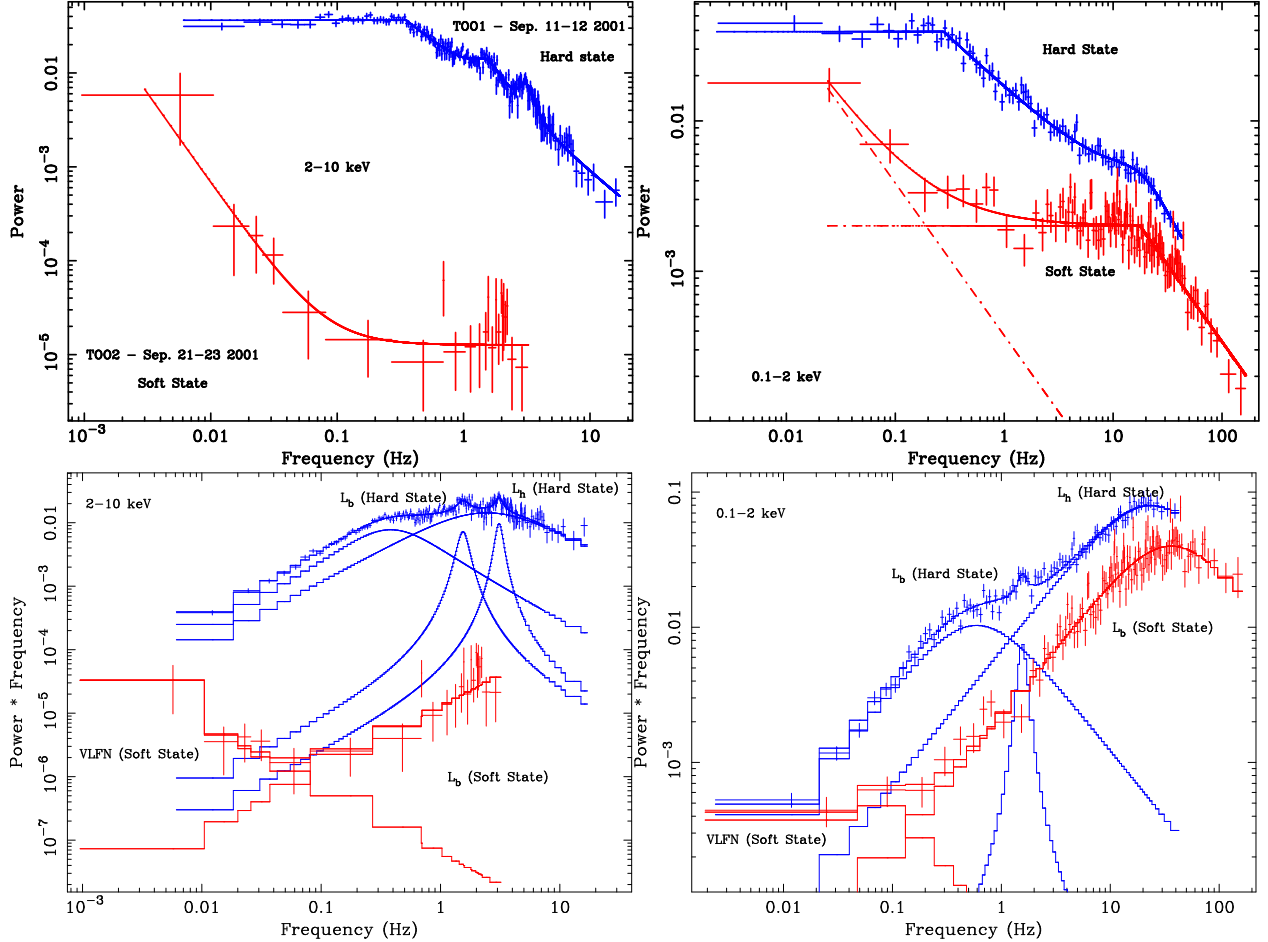


Fig. 6.— The LHS PS (blue) vs. HSS PS (red) for two different energy bands: 2-10 keV (*left panels*) and 0.1-2 keV (*right panels*). In the 2–10 keV, *top panels*: the HSS PS is fitted by the sum of a PL plus a CONSTANT (see Table 8), while the LHS PS is fitted by a BKNPL plus two Lorentzians (see Fig. 5); *bottom panel*, frequency \times power diagram: the HSS PS is fitted by the sum of two broad Lorentzians, while the LHS PS is fitted by the sum of 2 broad Lorentzians plus two narrow Lorentzians. It is apparent that the relative power of the HSS PS (with respect to the LHS PS) strongly depends on the energy band.

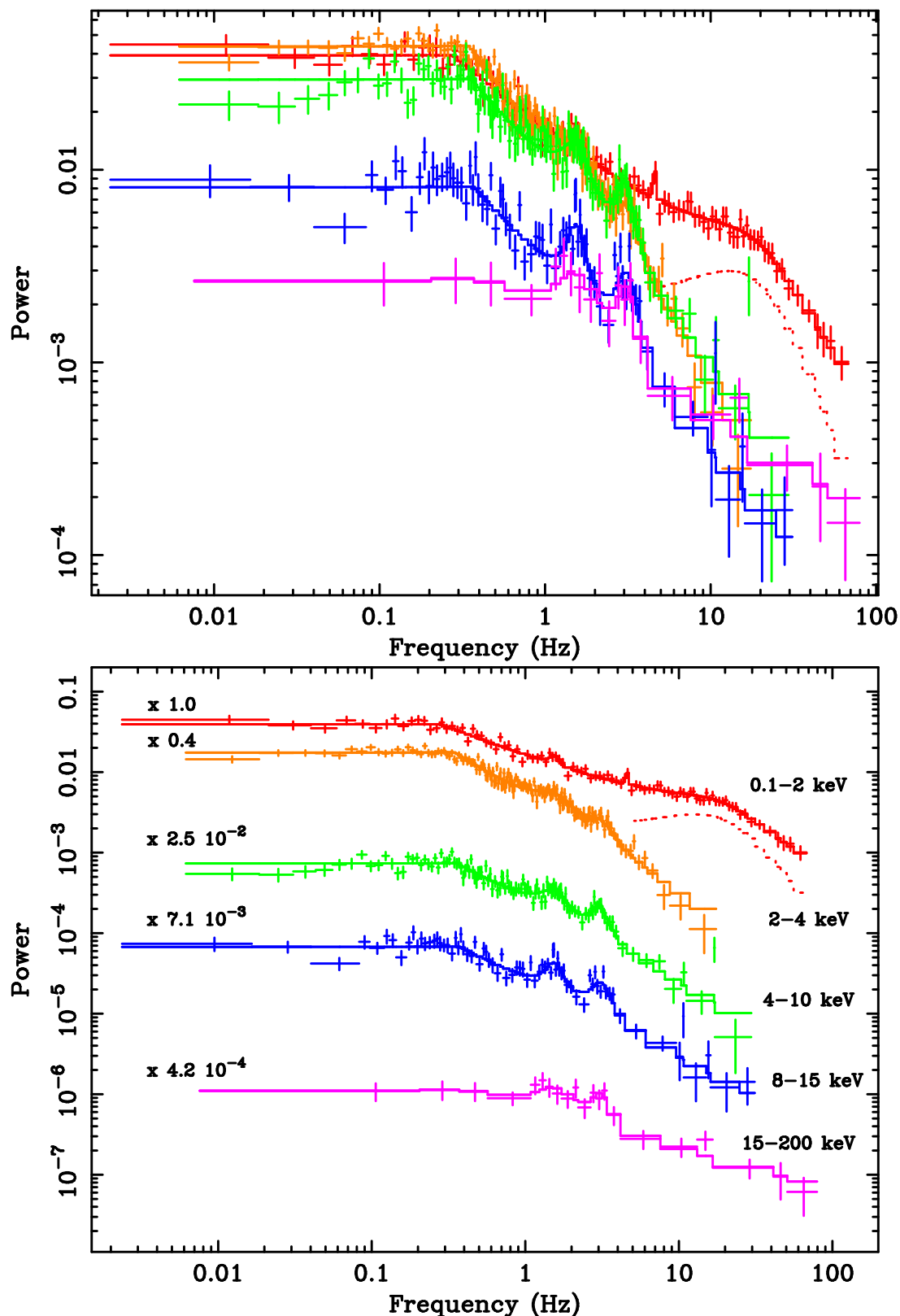


Fig. 7.— *Top panel:* the LHS power spectra in different energy bands (see bottom panel for the correspondence between color and energy intervals). The decrease of the variability power with energy is evident from this Figure. *Bottom panel:* the LHS power spectra as above, shifted, for clarity of display, along the ordinate direction by different factors, depending on the energy interval: factor 1 (0.1–2 keV), 0.4 (2–4 keV), 2.5×10^{-2} (4–10 keV), 7.1×10^{-3}

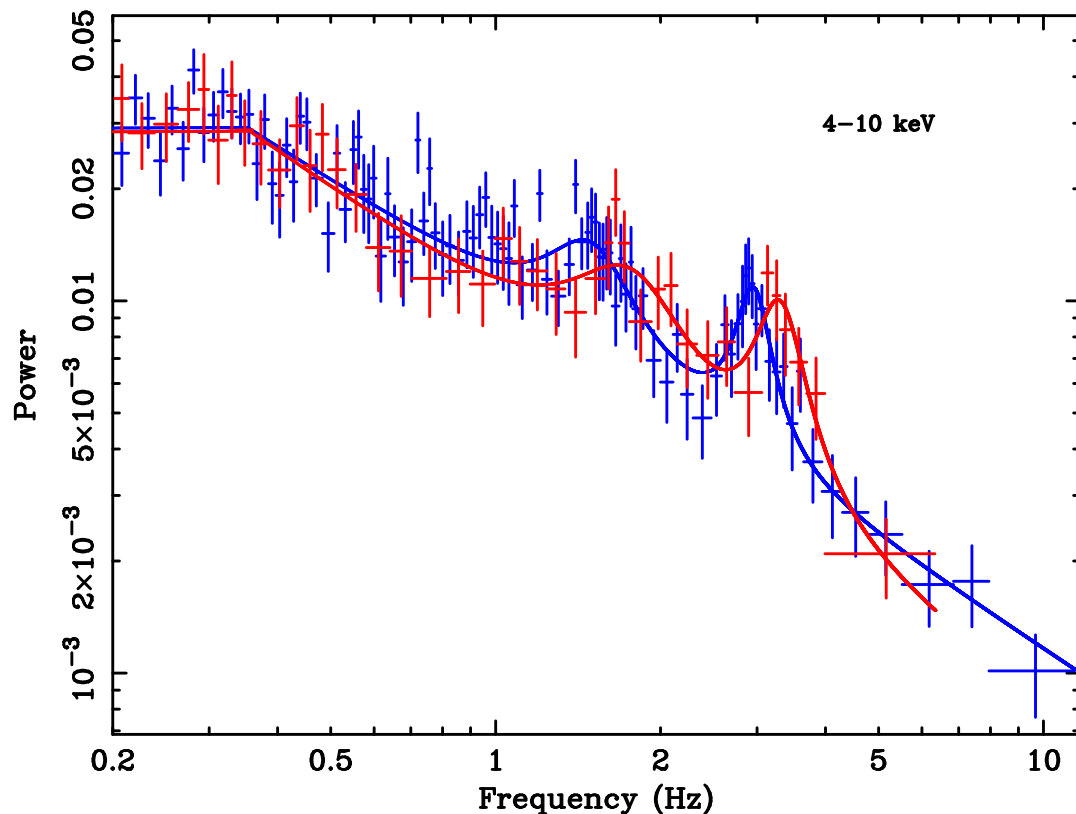


Fig. 8.— The LHS power spectra of XTE J1650-500 in the time intervals from I101 to I107 and from I109 to I112 (see text for details). The power spectrum (red line) corresponding to the softer energy spectrum is shifted to higher frequencies with respect to that (blue line) corresponding to the hard energy spectrum (see related energy spectra in Fig. 3). The fit with a BKNPL plus two Lorentzians is also shown. Best fit details in Table 6.

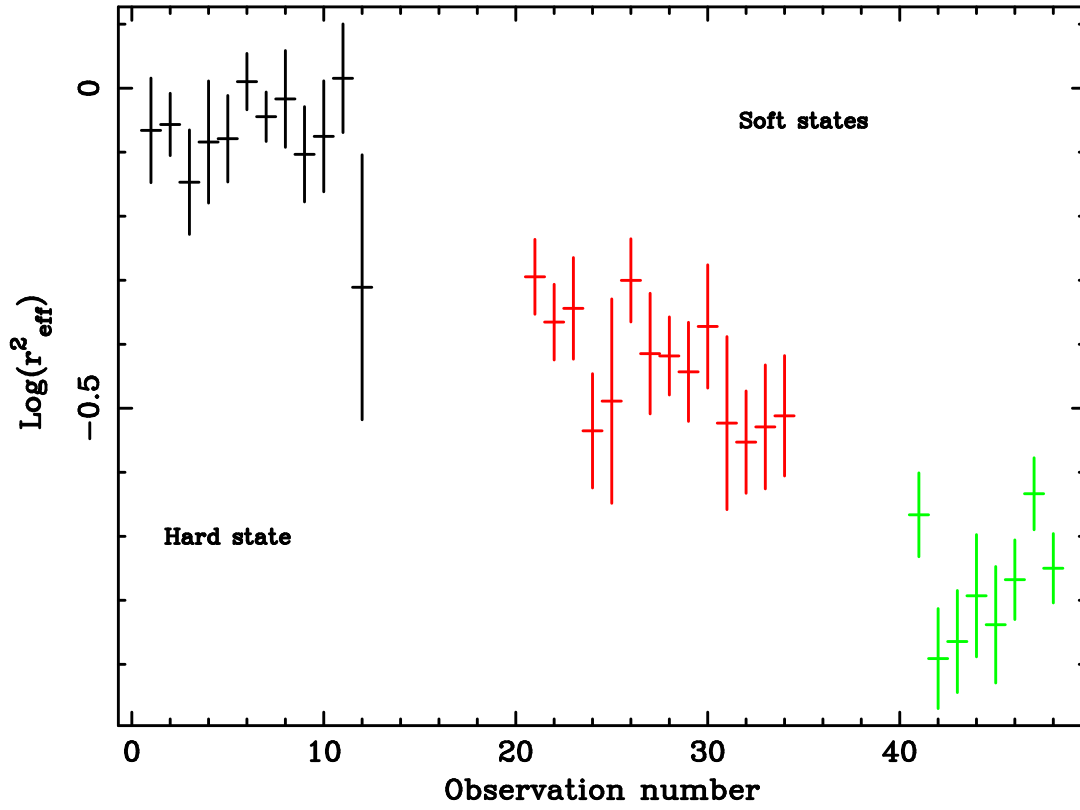


Fig. 9.— Evolution of the Compton cloud area during the spectral transition exemplified by the progressive number of the time intervals from TOO-1 to TOO-3 (see text). Colors correspond to TOO1 (black), TOO2 (red), TOO3 (green).

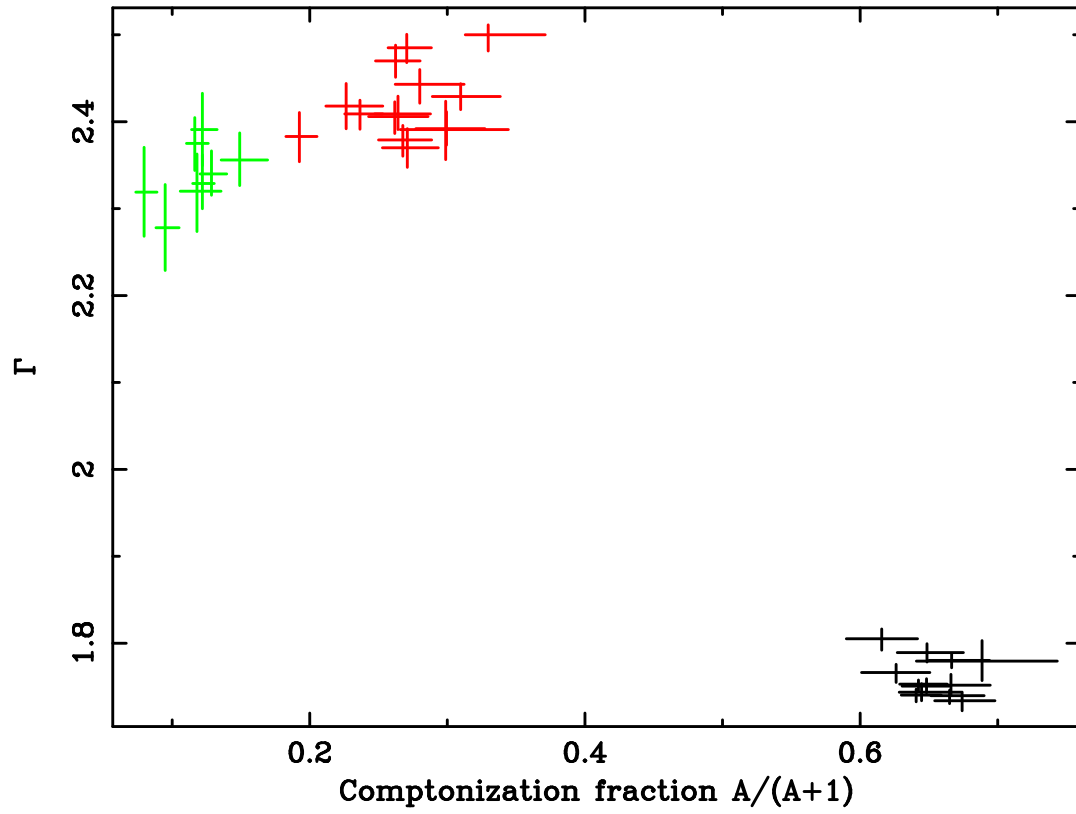


Fig. 10.— Evolution of the Comptonization fraction $f = A/(1+A)$ during the spectral transition from LHS to HSS. Colors correspond to TOO1 (black), TOO2 (red), TOO3 (green).